Numerical features of modeling plane wave diffraction by plasma microstructures employing the first Rytov approximation

S.Y. Gavrilov [1], A.I. Khirianova [1], E.V. Parkevich [1]
[1] P.N. Lebedev Physical Institute of the Russian Academy of Sciences,
119991, Russia, Moscow, Leninskiy Prospekt, 53

Abstract

In the study, we concern the features of modeling a diffraction equation obtained when solving the scalar Helmholtz wave equation in the parabolic and first Rytov approximations. The task is considered in the 2D case for a plane wave transmitted through a micron-sized plasma object. We develop a comprehensive guide for choosing optimal calculation conditions to make the employed modeling procedure be the most efficient and computationally inexpensive. Methods for controlling calculation errors are presented as well. The intensity and phase shift maps are simulated for the diffracted wave in the object's near-field region and analyzed in view of the observed regularities. The applicability of the parabolic and first Rytov approximations is examined in a numerical experiment depending on the radiation wavelength and object size. The results of the study can be useful to implement diffraction imaging techniques aimed at gaining insights into the optical properties of rapidly evolving phase objects.

Keywords: laser probing, plane wave diffraction, phase object, first Rytov approximation, near-field region, optical imaging.

Citation: Gavrilov SY, Khirianova AI, Parkevich EV. Numerical features of modeling plane wave diffraction by plasma microstructures employing the first Rytov approximation. Computer Optics 2026; 50(4): 1845. doi: 10.18287/COJ1845.

Acknowledgements: The study was supported by the Russian Science Foundation (Grant No. 24-79-10167).

Introduction

Nowadays, great emphasis is laid on the development of new computationally effective methods to study micron-sized phase objects encountered in various areas of fundamental and applied science. Here a special role belongs to the methods which involve diffraction imaging techniques implemented by using lens optical systems or systems based on lensless diffraction optics [1, 2]. By transmitting coherent laser radiation through a phase object and analyzing the changes in the field of the radiation passed through, one can evaluate or, in some cases, precisely retrieve the object's optical characteristics. Challenges in this regard arise when the object is small in size, evolves rapidly, and also has a complex structure. An example of such an object can be plasma microstructures often observed in studies of electrical discharges in liquids and gases [3, 4, 5, 6], laser sparks [7, 8, 9], plasma jets in plasma focus [10, 11], plasma ejections during laser ablation [12, 13, 14], shock waves [15, 16], turbulent flows of gas or liquid [17], complex condensed media [18], etc. The study of such objects by classical methods [19, 20], even when optical tomography methods are employed [21], becomes an extremely complex task, which in certain cases may be simply impossible. In this regard, modeling of both direct and inverse diffraction problems in the first Rytov approximation appears to be promising. This approximation is one of the asymptotic methods used to solve the scalar Helmholtz wave equation. The interest in this approximation, among all other existing ones [22, 23, 24, 25, 26], is owing to the fact that the diffraction equation obtained under this approximation appears to be sensitive to diffraction effects accompanying the passage of radiation through the phase object and outside it. Notably, the lack of consideration of diffraction effects can lead to incorrect results and ideas about the optical characteristics of the phase object under study. In addition, in recent studies [27, 28, 29], by using the first Rytov approximation, fundamental regularities in the visualization of phase objects in the field of coherent laser radiation were revealed. The results were of a general nature and allowed one even to construct an unambiguous solution to the inverse diffraction problem for the cases when the radiation absorption does or does not occur in the object [29]. The equations obtained were computationally inexpensive and represented a powerful tool for many optical studies. In view of the found features of the diffraction equation obtained in the first Rytov approximation and its important role in the development of new methods of diagnosing complex-structured rapidly evolving phase objects, which includes also laser diffraction tomography methods, it seems important to describe in detail all the aspects of its numerical modeling. Particular attention should be paid to the calculation errors and their accumulation on a scale of the employed computational grid together with the conditions under which the numerical results obtained satisfy the requirement of reliable convergence with not too many calculation iterations.

In contrast to previous studies focused on general theoretical principles and inverse problem solutions, the current work provides a detailed analysis of numerical aspects in modeling the direct diffraction problem within the first Rytov approximation. The key novelty of our research lies in developing a comprehensive practical guide for selecting optimal computational grid parameters and performing systematic error analysis. Specifically, we have systematized the requirements for spatial grid steps and established an empirical relationship between the size of the computational domain and both propagation distance and object radius. A thorough analysis of discretization and integration errors was performed using NRMSD metrics. We implemented a highly optimized Python algorithm employing FFT, enabling calculation of diffraction patterns in less than one second. The accuracy of the first Rytov approximation was quantitatively validated, demonstrating its adequacy for diagnosing plasma microobjects with less than 5% discrepancy compared to the second approximation in the near-field region. The obtained results provide a ready-to-use toolkit for processing diffraction patterns of rapidly evolving phase objects in plasma experiments.

1. Statement of the direct diffraction problem

Let us consider a plane wave $\sqrt{I_0}\exp(ikx)$, which has intensity I_0, wave vector modulus $k = 2\pi/\lambda$, and wavelength λ, probing a certain phase object along the $0x$ axis, see Fig. 1, with the object being surrounded by an infinite medium with a uniform dielectric permittivity equal to unity. The object's dielectric permittivity is $\varepsilon(x,\rho) = 1 + \tilde{\varepsilon}(x,\rho)$, where $\tilde{\varepsilon}(x,\rho)$ appears as the part that depends on the radiation frequency and is considered as a fluctuation relative to the environment, ρ is the two-dimensional variable introduced for the coordinates y and z in the coordinate system in Fig. 1.

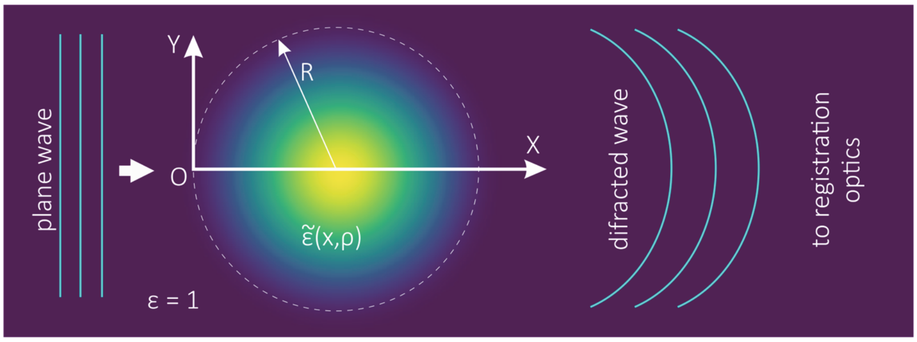

Fig. 1. Diffraction of a plane wave by a phase object

In this study, the analysis of the direct problem is based on the solution of the scalar Helmholtz wave equation [30]

$$\Delta U(x,\rho) + k^2(1 + \tilde{\varepsilon}(x,\rho))U(x,\rho) = 0, \quad (1)$$

where $U(x,\rho)$ is the complex amplitude of the wave field. Let us represent the wave field in the form of

$$U(x,\rho) = \sqrt{I_0}e^{\Phi(x,\rho)}, \quad (2)$$

by introducing a complex phase function $\Phi(x,\rho)$, which is defined as

$$\Phi(x,\rho) = ikx + i\delta\varphi(x,\rho) + \chi(x,\rho). \quad (3)$$

This function contains a phase shift $\delta\varphi(x,\rho)$, which is introduced by the phase object into the diffracted wave, the spatial intensity distribution $I(x,\rho)$ of the diffracted wave and a wave level $\chi(x,\rho) = \ln(\sqrt{I(x,\rho)/I_0})$ characterizing the changes in the wave intensity. In terms of the introduced functions, Eq. (1) takes the form

$$\Delta\Phi(x,\rho) + (\vec{\nabla}\Phi(x,\rho))^2 + k^2 + k^2\tilde{\varepsilon}(x,\rho) = 0, \quad (4)$$

where $\vec{\nabla} = \vec{h}_x\,\partial/\partial x + \vec{h}_y\,\partial/\partial y + \vec{h}_z\,\partial/\partial z$. Within the framework of Rytov's theory of wave diffraction, assuming that forward wave diffraction dominates, Eq. (4) can be reduced to a parabolic form

$$2ik\frac{\partial\Phi(x,\rho)}{\partial x} + \Delta_\perp\Phi(x,\rho) + (\vec{\nabla}_\perp\Phi(x,\rho))^2 + k^2\tilde{\varepsilon}(x,\rho) = 0, \quad (5)$$

where differentiation operators $\Delta_\perp = \partial^2/\partial y^2 + \partial^2/\partial z^2$ and $\vec{\nabla}_\perp = \vec{h}_y\,\partial/\partial y + \vec{h}_z\,\partial/\partial z$ are used. The further solution of Eq. (5) is based on the construction of an infinite series of the complex phase $\Phi = \Phi_0 + \Phi_1 + \Phi_2 + \ldots$ (the zeroth term corresponds to the undisturbed plane wave) and the employment of the smooth perturbation method. The solution of Eq. (5) itself is presented in the form of an infinite system of iterative equations, in which each subsequent term with a decreasing magnitude is determined through the previous one, see the details in the original study [31]. Notably, the assumption that forward wave diffraction dominates is closely related to the parabolic approximation of the Helmholtz wave equation. From a mathematical point of view, the condition for its applicability consists in the relative smallness of the partial derivatives $|\lambda\,\partial U(x,\rho)/\partial x| \ll |U(x,\rho)|$ and $|\lambda\,\partial^2 U(x,\rho)/\partial^2 x| \ll |\partial U(x,\rho)/\partial x|$ introduced for the complex amplitude of the wave field and considered along the direction of its propagation. Obviously, such conditions can be fulfilled only if the backscattered field is small, which is characteristic of many phase objects.

In the current research, we are interested in the solution of Eq. (5) in the first approximation corresponding to the first term of the infinite series of the complex phase function. With this approximation, the solution of Eq. (5) is found as

$$\Psi_1(x, f_\rho) = -\frac{k}{2i}\int_0^x \exp(-i\lambda\pi(x-x')f_\rho^2)\Lambda(x', f_\rho)\, dx', \tag{6}$$

wherein functions $\Psi_1(x, f_\rho)$ and $\Lambda(x, \rho)$ are defined as follows

$$\Psi_1(x, f_\rho) = \iint_{-\infty} \Phi_1(x, \rho)\exp(-2\pi i\rho f_\rho)\, d\rho^2, \tag{7}$$

$$\Lambda(x, f_\rho) = \iint_{-\infty} \tilde{\varepsilon}(x, \rho)\exp(-2\pi i\rho f_\rho)\, d\rho^2. \tag{8}$$

The variable f_ρ appears as the two-dimensional variable introduced for the variable ρ. Note that functions $\Lambda(x, f_\rho)$ and $\Psi_1(x, f_\rho)$ themselves do not present the direct Fourier transforms. In essence, e.g., function $\Lambda(x, f_\rho)$ appears as a set of the Fourier spectra obtained for each section of function $\tilde{\varepsilon}$ having the longitudinal coordinate of x.

The Eq. (6) takes into account the diffraction spreading of the wave during its passage through the object and behind its output plane, and also allows one to describe the wave propagation behind the object at distances that satisfy the criteria for the applicability of the first Rytov approximation

$$\lambda(x-x')/l_{\tilde{\varepsilon}}^2 \ll (l_{\tilde{\varepsilon}}/\lambda)^2. \tag{9}$$

Here parameter x is the distance at which the diffracted wave is considered behind the object. The inequality (9) should be fulfilled to provide for a parabolic form of the Helmholtz wave equation [31]. Apart from this, in Rytov's theory of wave diffraction, it is required that the minimum spatial scale $l_{\tilde{\varepsilon}} \sim \tilde{\varepsilon}/|\vec{\nabla}\tilde{\varepsilon}|$ (where $\vec{\nabla} = \vec{h}^x\,\partial/\partial x + \vec{h}^y\,\partial/\partial y + \vec{h}^z\,\partial/\partial z$) of the changes in the fluctuation part $\tilde{\varepsilon}$ of the object dielectric permittivity significantly exceeds the radiation wavelength λ. This condition is basic for the applicability of the smooth perturbation method used to construct the complex phase series expanded by a small parameter. The latter is considered as the dispersion $\sigma_{\tilde{\varepsilon}} = \sqrt{\langle\tilde{\varepsilon}^2\rangle} = \sqrt{\langle[\tilde{\varepsilon} - \langle\tilde{\varepsilon}\rangle]^2\rangle}$ of the function $\tilde{\varepsilon}$. Here we have the symbol $\langle\ldots\rangle$ that means averaging, and $\langle\tilde{\varepsilon}\rangle = 1/V\int_V \tilde{\varepsilon}dV$, which denotes the mean value obtained for the function $\tilde{\varepsilon}$ given in the volume V. Indeed, the value of $\sigma_{\tilde{\varepsilon}}$ should satisfy the condition

$$\langle|\vec{\nabla}_\perp\Phi_1|^2\rangle = 1/V\int_V |\vec{\nabla}_\perp\Phi_1|^2 dV \ll k^2\sigma_{\tilde{\varepsilon}}, \tag{10}$$

where function Φ_1 is given by Eq. (3), and $\vec{\nabla}_\perp = \vec{h}_y\,\partial/\partial y + \vec{h}_z\,\partial/\partial z$. The fulfillment of condition (10) ensures the convergence of the infinite series of a complex phase.

The conceptual error of the first Rytov approximation is considered with respect to the characteristic value of the second term of the Rytov's series, which is called the second Rytov approximation and given by the following equations

$$X(x, \rho) = \iint_{-\infty} \left(\vec{\nabla}_\perp\Phi_1(x, \rho)\right)^2 \exp\left(-2\pi i\rho f_\rho\right) d\rho^2, \tag{11}$$

$$\Psi_2(x, f_\rho) = -\frac{1}{2ik}\int_0^x X(x', f_\rho)\exp\left(-i\lambda\pi(x-x')f_\rho^2\right)dx'. \tag{12}$$

Based on Eqs. (6) and (12), we obtain the resultant phase shift $\delta\phi = \delta\phi_1 + \delta\phi_2$ and intensity $I = I_0 \times I_1 \times I_2$ of the diffracted wave, the terms of which are defined as $\delta\phi_{1,2}(x, \rho) = \mathrm{Im}(\mathcal{F}^{-1}\{\Psi_{1,2}(x, f_\rho)\})$ and $I_{1,2}(x, \rho) = \exp\left(2 \times \mathrm{Re}(\mathcal{F}^{-1}\{(\Psi_{1,2}(x, f_\rho)\})\right)$, wherein the symbol $\mathcal{F}^{-1}$ denotes the application of the inverse Fourier transform. Hereinafter, the value of I_0 is taken to be equal to unity, since we consider relative changes in the diffracted wave characteristics.

Below, we analyze both terms of the Rytov series, but the most attention is paid to the first one, since it is the key approximation in solving the direct and inverse diffraction problems. Also, in the study, we numerically simulate all the considered equations by using the Python programming language, so the features of the computation tasks are addressed to this language exclusively.

2. Numerical investigations

2.1. Model of a plasma microstructure

As a model object, for which the direct diffraction problem is simulated, we take a thin plasma cylinder (filament), the characteristics of which are taken as close as possible to those of plasma microstructures studied in [32]. The filament is probed by laser radiation (in the plane wave approximation) at $\lambda = 532$ nm. The filament's diameter is $2R = 20$ µm, and its electron density profile has the form of $n_e(\rho) = A(1 + \cos(\pi\rho/R))/2$, wherein $\rho = \sqrt{(x-R)^2 + y^2}$; the profile has axial symmetry at $x = R$. Parameter $A = 5 \times 10^{19}$ cm $^{-3}$ is the dimension factor. The dispersion part of the filament's dielectric permittivity is defined as $\tilde{\varepsilon} = -\omega_{pe}^2/\omega^2$, where $\omega_{pe} = (4\pi e^2 n_e/m_e)^{1/2}$ (e and m_e are the electron charge and mass) and ω are the plasma and radiation frequencies.

For the considered model of a phase object (plasma), the ratio between the left and right sides of the inequality (10), obtained for the region of 20 µm (along the 0x axis) and 30 µm (along the 0y axis) for the plasma filament 20 µm in diameter with the electron density profile described by the cosine law, is 0.36 %. This predicts a high accuracy of modeling plane wave diffraction by the object (inside it) in the first Rytov approximation. Without reducing the generality of Rytov's theory of wave diffraction, we mention that the considered diffraction equations themselves are of a general character and allow one to evaluate wave diffraction by a wide range of phase objects.

2.2. Approximation of the electron density distribution

In terms of a single program code, the two-dimensional distribution of the filament's electron density was defined in the numpy library as an array of zeros, onto which a logical mask with the electron density distribution was imposed, allowing one to reach the axial symmetry for the distribution. Such an approach significantly reduces the time required to create an appropriate electron density profile compared to nested cycles usually used in this task. Also, in the code algorithms, the coordinate grid $X, Y = np.meshgrid(x, y)$ is employed to simplify the determination of the variable $\rho = \sqrt{(x-R)^2 + y^2}$.

Let us switch from a continuous distribution of the electron density to a discrete one and find an optimal spatial step of the computational grid that does not entail significant discretization errors. Obviously, for this case the condition $dx, dy \ll 2R$ should be satisfied. Let us define the electron density function on a scale of 20×20 μm ^{2} $(2R \times 2R)$. Fig. 2*a* demonstrates the computed relative root-mean-square error of the linear approximation (normalized root-mean-square difference) of the electron density function depending on the spatial step Δ of the uniform grid, which, for a fixed scale of the computational zone $\Delta X \times \Delta Y$, is uniquely determined by the number of points N^2 taken along the Ox and Oy axes

$$NRMSD[n_e(x,y)_N, n_e(x,y)_{N-1}] = \frac{\sqrt{\frac{1}{N}\sum_{i,k=0}^{N}[n_e(x_i y_k)_N - n_e(x_i y_k)_{N-1}]^2}}{\frac{1}{N}\sum_{i,k=0}^{N} n_e(x_i y_k)_N}. \quad (13)$$

In the calculation, the value of Δ was varied from $2R/4$ to $2R/100$ by changing the point number N. Based on the data in Fig. 2*a*, we take a step equal to $\Delta = 0.75$ μm, with an approximation error of the object electron density being of $NRMSD[n_e(x,y)_N, n_e(x,y)_{N-1}] = 1\%$ (≈ 0.25 μm). This value seems to be a completely acceptable numerical result from an experimental point of view. Notably, in a general case, the value of the optimal step of the computational grid depends on the size of a considered model object. It is seen in Fig. 2*b* that, as the object size increases, the maximum step of the uniform grid also increases, and this increase is linear; see Fig. 2*c*.

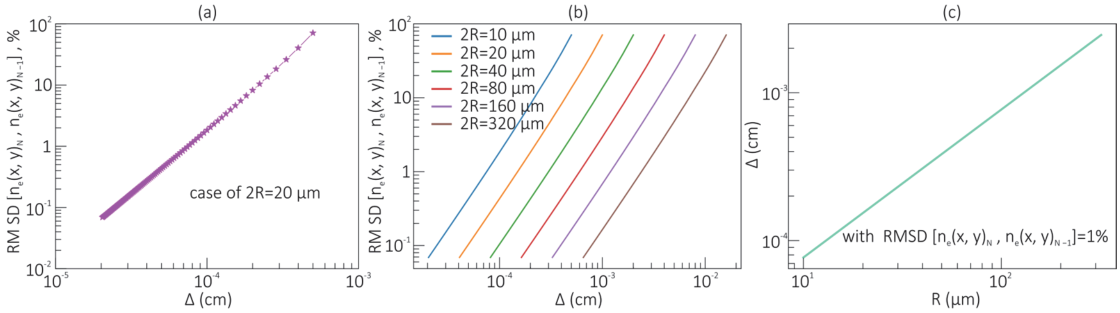

Fig. 2. (a) Error $NRMSD[n_e(x,y)_N, n_e(x,y)_{N-1}]$ of approximating electron density $n_e(x,y)$ of a plasma filament 20 μm in diameter on the scale of 20×20 μm depending on spatial grid step Δ.

2.3. Selecting the grid size in a transverse direction

Following the calculations in the previous section 3.2, we select the step of the computational grid equal to $\Delta = 0.25$ μm, and limit the modeling zone to a square frame of 500×1000 μm ^{2}, having previously checked that with this size there is no overlapping of the Fourier spectra due to the insufficient size of the Fourier transform window. This effect manifests itself in the form of reflections of the diffracted wave from the frame boundaries. Note that here we are proceeding from a typical picture of 2D diffraction patterns of an object, which will be described below.

Let us simulate the wave field behind the object at a distance of 500 μm measured from its input plane (with the coordinate of $x = 0$) for different radii of the object without changing the key parameters of the numerical calculation. In the procedure, we define the following distances (Fig. 3*a*):

$$\frac{2\int_{-\infty}^{-y_{max}}|I - I_0|dy}{\int_{-\infty}^{\infty}|I - I_0|dy} = 1\%; 0.1\%; 0.01\% \quad (14)$$

where y_{max} can correspond to $\Delta y_{1\%} = y_{1\%} - y_0$, $\Delta y_{0.1\%} = y_{0.1\%} - y_0$, and $\Delta y_{0.01\%} = y_{0.01\%} - y_0$, where $y_{1\%}$, $y_{0.1\%}$, and $y_{0.01\%}$ are considered relative to the point $y = 0$. In the expressions, the parameter $I_0 = 1$ denotes the incident plane wave intensity. In addition, we determine the distance $\Delta y_{first\ max}$ and $\Delta y_{second\ max}$ measured from the symmetry center of the object's diffraction pattern (coincides with the Ox axis passing through the coordinate system origin) and the very first maximum $I_{first\ max}$ and the second maximum $I_{second\ max}$ of the diffracted wave intensity (Fig. 3*e*).

In Fig. 3*a-e* one can analyze the behavior of the indicated distances under different conditions of the numerical simulation. Here, we start with the distance $\Delta y_{0.01\%}$, which limits the peripheral region wherein the changes in the diffracted wave intensity (small-scale fluctuations of the intensity profile) are higher than 0.01% of the incident plane wave intensity. The curve 1 in Fig. 3*a* shows that for objects with a radius of $R \sim 5 - 40$ μm the minimum size of the transverse grid ΔY should be chosen inversely proportional to the radius of the object R, whereas for objects with $R >$

40 μm the grid size can be taken proportional to R. The curve 1 in Fig. 3*e* shows that at $R \sim 5-20$ μm the position of the main maximum of the diffraction pattern is practically independent of the value of the diffraction cone angle and increases linearly with its increase at $R > 20$ μm. The position of the second maximum (curve 2) of the diffraction pattern increases linearly with its increase over the entire range. The general tendency of increasing the distance between the Oy axis and the position of the first predetermined intensity integral deviation is due to the influence of the geometric size of the object. Fig. 3*b* shows that, as the distance x increases, the distances $\Delta y_{1\%}$, $\Delta y_{0.1\%}$, $\Delta y_{0.01\%}$, and $\Delta y_{first\ max}$ rise almost linearly.

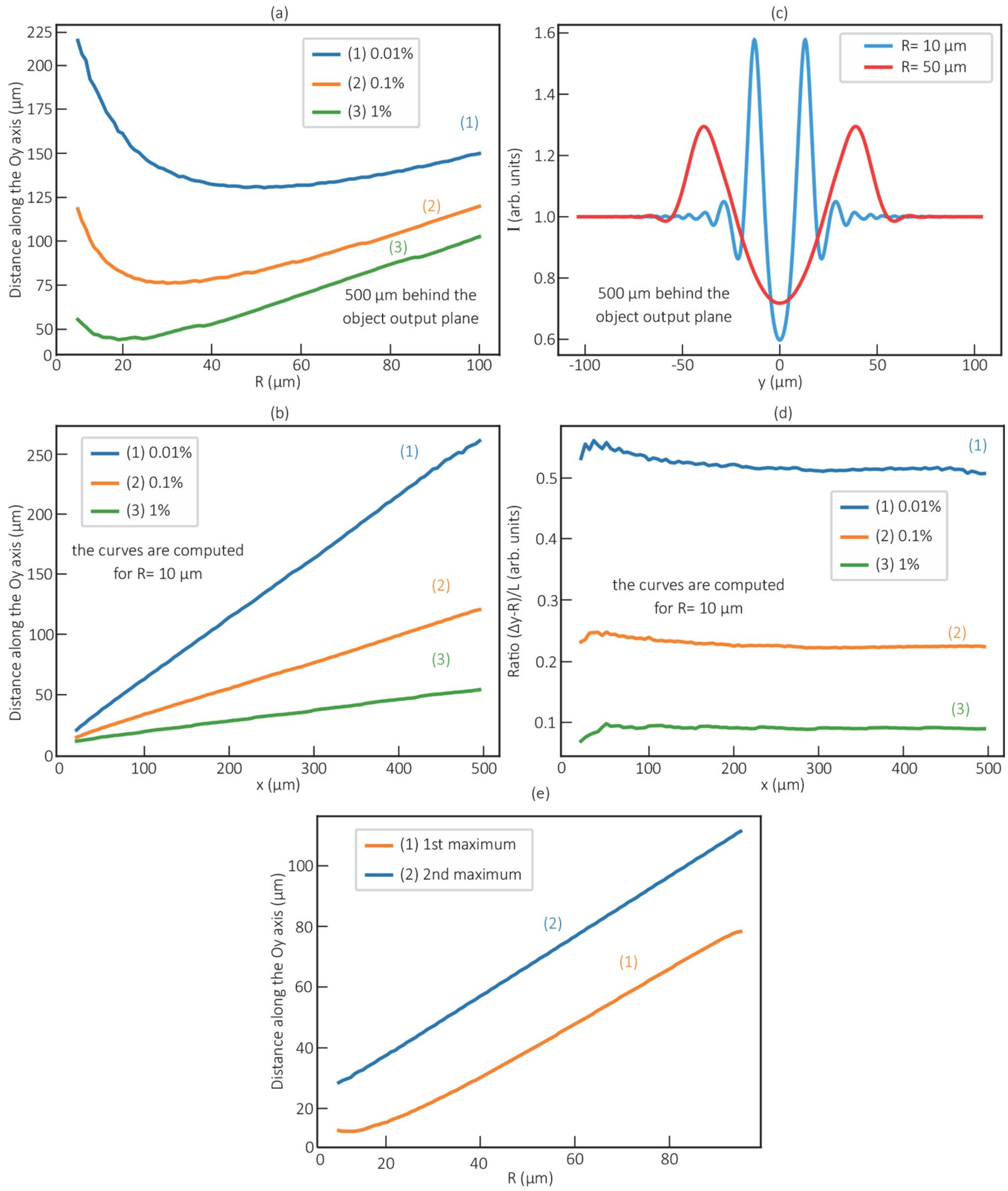

Fig. 3. Distances $\Delta y_{1\%}$, $\Delta y_{0.1\%}$, and $\Delta y_{0.01\%}$ measured from the Oy axis characterizing the changes in the diffracted wave intensity in various percentages

Fig. 3*d* shows the behavior of the slope coefficients of the considered curves 1–3 in Fig. 3) and 3*b*, with the deduction of the object's linear size (its radius) taken into account. It is evident that, starting from a certain distance x, for various predetermined intensity deviations (in percentage terms), a linear relationship is found between the values $\Delta y_{1\%}$, $\Delta y_{0.1\%}$, and $\Delta y_{0.01\%}$ and the value of the propagation distance x of the diffracted wave. The distributions in Fig. 3(*d*) predict that the position on the Oy axis at which the amplitude of the diffracted wave intensity changes for the last time (relative to the $y = 0$ point axis) by a value not greater than 0.1% (relative to the unit level) can be described by the following empirical expression $\approx 0.23 \times x + R$. Accordingly, the minimum size of the computational grid in the periphery of ΔY can be defined as $2 \times (0.23 \times x + R)$.

The obtained result is consistent with those of many numerical simulations carried out for different values of ΔY, when the effects of wave reflection from the edges of the computational domain appear. Mention that the information presented in this subsection gives an exhaustive guide for the further determination of the transverse size of the computation grid in the considered modeling task.

2.4. Implementation of Fourier transforms

In order to implement the Fourier transforms in the diffraction equations, a transition was made from the integral transform to the discrete one by using the Cooley-Tukey fast Fourier transform algorithm. In the Python language, the fast Fourier transform procedure is implemented in the numpy.fft and scipy.fft libraries. In the study, we use the numpy.fft library, since it showed the highest calculation speed during the modeling of the diffraction problem. Also, to reach a minimum calculation time, the optimal number of points on the Oy axis (on which the direct and inverse Fourier transforms are computed) is taken as a multiple of two, since the Cooley-Tukey algorithm operates faster with such values.

The numpy.fft library implements the two-dimensional discrete Fourier transform according to the formula $\sum_{m=0}^{n-1} a_m \exp(-2\pi i \frac{mj}{n})$, where a_m are the values at the nodes of the considered function to which the direct Fourier transform is applied, $j = [0; n-1]$, and n is the number of a point on the coordinate axis. Let us pay attention to the fact that spatial frequencies in the library have a normalization factor of 2π, whereas, e.g., in expressions (7) and (8) this factor is absent, since we operate directly with the spatial frequencies f_y and f_z. The amplitude of the calculated spectrum in such a library is normalized to the number of points used. However, due to the linear dependence of integrals (7) and (8) on the value of the two-dimensional spectrum $\Lambda(x', f_\rho)$ and for a regular computation grid (if the integration step dx does not change along the $0\mathrm{x}$ axis), the mentioned features are eliminated when applying the inverse Fourier transform to the function $\Psi_1(x, f_\rho)$.

In order to accelerate the Fourier transform, the latter is performed without using the cycle for, but with the $(\mathrm{axis} =)$ axis specified as an argument to the np.fft.fft() function. Arrays of zeros *numpy* are set up for further numerical calculation of integral (6) using the trapezoidal method. To speed up calculations, constants, which do not change in the code cycle, are computed outside the cycle. The np.cumsum() function is used, which allows one to significantly increase the speed of modeling integral (6) without deteriorating the accuracy of the performed calculations. When calculating the phase shift and intensity of the diffracted wave, the inverse Fourier transform applied to function $\Phi_1(x, f_\rho)$ given by Eq. (6) is also computed without using the cycle *for*, but with the $(\mathrm{axis} =)$ axis specified.

2.5. Numerical integration method

Let us consider integral equation (6) in the form of

$$\Psi_1(x, f_\rho) = -\frac{k}{2i}\exp(-i\lambda\pi x f_\rho^2)\int_0^x \exp(i\lambda\pi x' f_\rho^2)\Lambda(x', f_\rho)\, dx'. \quad (15)$$

The spectrum $\Lambda(x, f_\rho)$ can have a rather complex dependence on the longitudinal coordinate x, and, in a general case, it is impossible to analytically simulate integral (15). We compute this integral numerically employing the trapezoid method, which seems to be the simplest one in terms of its implementation and provides reliable results characterizing the diffraction patterns of the probed object. According to the method, integral (15) is replaced by an approximate sum

$$\Psi_{n,\beta} = -\frac{k}{2i}\sum_{\alpha=1}^{n}\frac{\exp(i\lambda\pi(x'_\alpha - x_n)f_{\rho_\beta}^2)\Lambda_{\alpha,\beta} + \exp(i\lambda\pi(x'_{\alpha-1} - x_n)f_{\rho_\beta}^2)\Lambda_{\alpha-1,\beta}}{2}\Delta x. \quad (16)$$

Here we have $\alpha = [1; n]$, with n being the summation index introduced for points on the $0\mathrm{x}$ axis, β denotes the summation index related to the points on the $0\mathrm{y}$ axis, $\Psi_{\mathrm{n},\beta}$ is the function value in the point with the coordinates (n, β). Let us transform expression (16) by taking the exponent outside the summation

$$\Psi_{n,\beta} = -\frac{k}{2i}\exp(-i\lambda\pi x_n f_{\rho_\beta}^2)\sum_{\alpha=1}^{n}\frac{\exp(i\lambda\pi x'_\alpha f_{\rho_\beta}^2)\Lambda_{\alpha,\beta} + \exp(i\lambda\pi x'_{\alpha-1} f_{\rho_\beta}^2)\Lambda_{\alpha-1,\beta}}{2}\Delta x. \quad (17)$$

By dividing the expression under the summation sign into two parts and getting rid of the differences in the summation indices along for the $0\mathrm{x}$ axis, we obtain

$$\Psi_{n,\beta} = -\frac{k}{2i}\exp(-i\lambda\pi x_n f_{\rho_\beta}^2)\left(\sum_{\alpha=1}^{n}\frac{\exp(i\lambda\pi x'_\alpha f_{\rho_\beta}^2)\Lambda_{\alpha,\beta}}{2} + \sum_{\alpha=0}^{n-1}\frac{\exp(i\lambda\pi x'_\alpha f_{\rho_\beta}^2)\Lambda_{\alpha,\beta}}{2}\right)\Delta x. \quad (18)$$

Let us select the common identical part of both obtained sums and take the terms, which correspond to the differences in the sums, out of the summation sign, as well as sum the remaining parts with each other. As a result, we get the following formula for numerical calculations

$$\Psi_{n,\beta} = A_\beta\left(\sum_{\alpha=1}^{n-1}\psi_{\alpha,\beta} + \frac{\psi_{0,\beta} + \psi_{n,\beta}}{2}\right)\Delta x, \quad (19)$$

wherein $A_\beta = -\frac{k}{2i}\exp(-i\lambda\pi x_n f_{\rho_\beta}^2)$ and $\psi_{\alpha,\beta} = \exp(i\lambda\pi x'_\alpha f_{\rho_\beta}^2)\Lambda_{\alpha,\beta}$.

Note that the simulation error of modeling integral (6) by using the trapezoid method decreases quadratically as the grid step Δx decreases. At the same time, the step cannot be infinitely reduced because of the accumulation of rounding errors.

2.6. Selecting the computation grid step along the Ox and Oy axes

Let us consider the influence of the spatial step of the computational grid on the accuracy of calculating the object diffraction patterns employing the formula (19). For simplicity, we limit ourselves to brightness patterns obtained in terms of the changes in the diffracted wave intensity. To determine the optimal spatial step of the computational grid, we select a modeling region with the size of 300×170 µm, where the transverse size of the region is selected on the basis of the empirical regularity described in subsection 3.3. In the modeling, we take the grid step along the $\mathrm{O}y$ axis to be equal to $\Delta y = 0.75$ µm that, according to the results of subsection 3.2, is sufficient for a reliable description of the plasma microstructure. The changes in the diffracted wave field are considered far from the object in the plane with the coordinate of $x = 300$ µm.

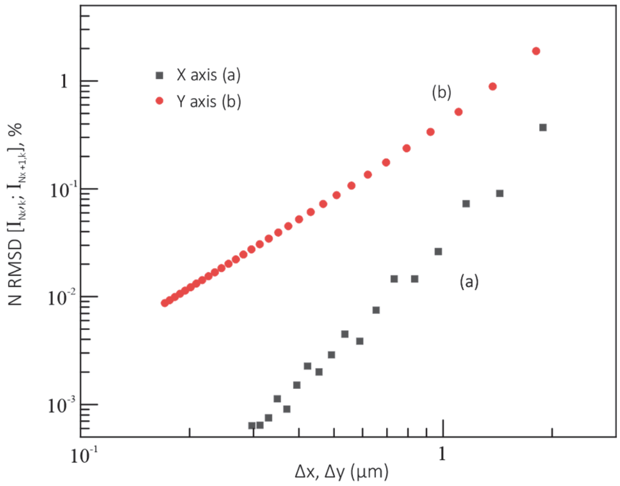

Fig. 4. Errors $NRMSD[I_{N_x,k}; I_{N_x+1,k}]$ (a) and $NRMSD[I_{N_y,k}; I_{N_y+1,k}]$ (b) of calculating the object's brightness diffraction patterns far from its output plane depending on the computation grid step: (a) along the Ox axis with the fixed $\Delta y = 0.75$ µm and (b) along the Oy axis with the fixed $\Delta x = 0.75$ µm

The variation of the computational grid step, e.g., along the $\mathrm{O}x$ axis, leads to certain discrepancies in the intensity calculated far from the object. Let $I_{N_x,k}$ and $I_{N_x+1,k}$ be the diffracted wave intensities calculated with different spatial steps of the grid. Here k is the index corresponding to the position of the value $I_{N_x,k}$ on the $\mathrm{O}y$ axis, and N_x is the number of points determined on the Ox axis. For the selected scale of the computational zone $\Delta X \times \Delta Y$, the value of N_x determines the spatial step Δx, respectively. To describe the influence of the spatial step of the computational grid on the accuracy of calculating the brightness diffraction patterns of the object, we introduced the following formula

$$NRMSD[I_{N_x,k}; I_{N_x+1,k}] = \frac{\sqrt{\frac{1}{N_y}\sum_{k=0}^{N_y}((I_{N_x+1,k}-1)-(I_{N_x,k}-1))^2}}{\frac{1}{N_y}\sum_{k=0}^{N_y}(|I_{N_x,k}-1|)}. \quad (20)$$

Notably, when comparing $I_{N_x,k}$ and $I_{N_x+1,k}$, it is necessary to vary the point number along the coordinate axis, not the length of the spatial step. For instance, if a spatial step length is used, a situation may occur when different step lengths correspond to an equal number of points due to the translation of the ratio of the grid size to the step length into an integer. When such a situation arises, the error calculation according to formula (19) can entail anomalies in the behavior of the error $NRMSD[I_{N_x,k}; I_{N_x+1,k}]$, however, the general tendency of increasing the accuracy of the numerical calculation with a decrease in the spatial step remains unchanged.

Similarly, the function $NRMSD[I_{N_y,k}; I_{N_y-1,k}]$ (the step along the Ox axis is fixed) can be introduced

$$NRMSD[I_{N_y,k}; I_{N_y-1,k}] = \frac{\sqrt{\frac{1}{N_y}\sum_{k=0}^{N_y}((I_{N_y,k}-1)-((I_{N_y-1,k})_{interpolated}-1))^2}}{\frac{1}{N_y}\sum_{k=0}^{N_y}(|I_{N_y,k}-1|)}. \quad (21)$$

To correctly compare the field distributions along the Y-axis as the number of points along this axis was increased, linear interpolation was applied using the unterp1d function from the scipy.interpolate library. The calculated distributions $NRMSD[I_{N_x,k}; I_{N_x+1,k}]$ and $NRMSD[I_{N_y,k}; I_{N_y+1,k}]$ are shown in Figs. 4*a* and 4*b*.

The general trend in the behavior of the computation errors $NRMSD[I_{N_x,k};\ I_{N_x+1,k}]$ and $NRMSD[I_{N_y,k}; I_{N_y+1,k}]$ reveals a good convergence of the solution of the considered direct diffraction problem in the near-field region with a decrease in the spatial step of the computational grid both along the Ox and Oy axes. In this case, from the point of view of the calculation accuracy and speed, the optimal spatial step for both axes constitutes $\Delta x = \Delta y = 0.75$ μm.

3. Computation results

3.1. Brightness and phase shift diffraction patterns of the plasma filament

Fig. 5*a* and 5*b* show the modeling results obtained for the direct diffraction problem described by Eq. (6) at a distance of up to 500 μm behind a plasma filament with the radius of $R = 20$ μm. The graphs in Figs. 5 and 5*d* are obtained in terms of the second Rytov term and supplement the data in figs. 5*a* and 5*b*. The maps were obtained with $\Delta Y = 270$ μm and $\Delta x = \Delta y = 0.75$ μm. The time for calculating maps using the algorithms described above was less than one second.

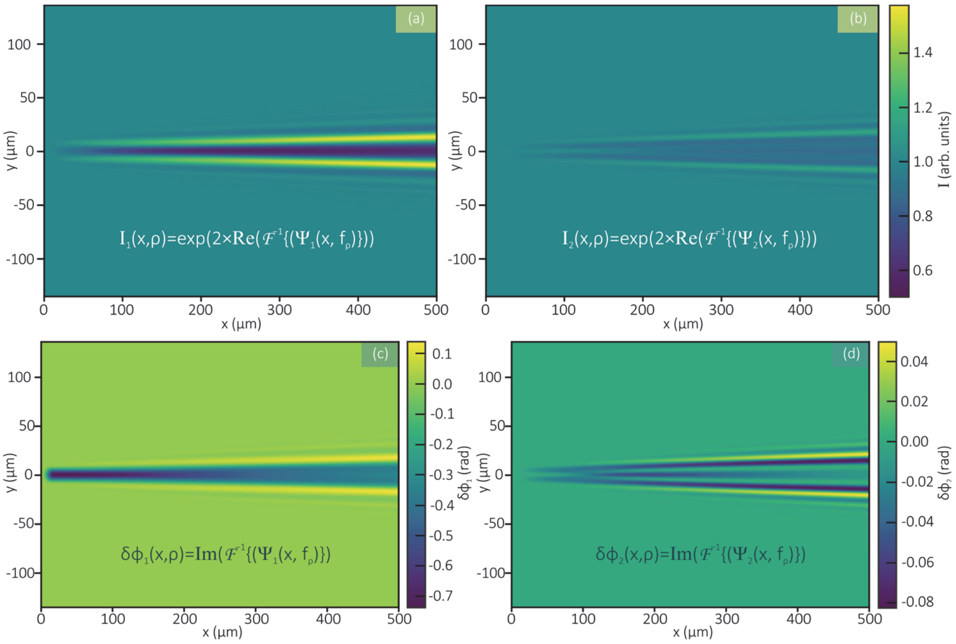

Fig. 5. Brightness (a,b) and phase (c, d) maps of the wave diffracted by the plasma filament 20 μm in diameter. The maps are obtained in the first (a, c) and second (b,d) Rytov approximations

One can see that wave diffraction by the plasma filament leads to the appearance of numerous fluctuations in the wave intensity and its phase shift. The resultant intensity pattern, see Fig. 5(*a*), reveals a sharp drop in the wave intensity behind the object enhancing along the Ox axis. This effect can be explained by the fact that the propagation of the wave through the plasma cylinder, which has a lower refractive index than that of the surrounding medium, is equivalent to scattering on a negative cylindrical lens. The negative phase shift, which occurs when the wave passes through the object, see Fig. 5(*b*), is stipulated by the fact that the wave phase velocity in the plasma medium is higher than the speed of light in air. At the same time, in the near-field region of the plasma filament, wave diffraction results in the appearance of positive fluctuations of the phase shift. In the image processing procedure and with no prior information about such a feature, this can lead to incorrect results if the local zones with the positive phase shift are treated as the gas compression (emergence of a shock wave). As the wave propagates along the Ox axis, the amplitudes of high diffraction orders increase in the intensity map, because of the energy redistribution of the electromagnetic wave field in the periphery, whereas the resultant wave energy remains constant.

3.2. The error of the first Rytov approximation in terms of calculating the second Rytov term

In many studies, when expanding a function into an infinite series with terms whose amplitude decreases with increasing ordinal number of the term, the second term of the series is considered as the error of the first term. Such an approach is relevant, but one needs to numerically investigate the discrepancy between the first Φ_1 and second Φ_2 terms of the complex phase series as a function of the distance x traveled by the diffracted wave. The corresponding discrepancies are clearly indicated in Figs. 6(a) and 6(b) by the profiles of the functions $I_{1,2}(x,y) = I_1(x,y) \times I_2(x,y) - I_1(x,y)$ and $\delta\phi_{1,2}(x,y) = \delta\phi_1(x,y) + \delta\phi_2(x,y) - \delta\phi_1(x,y) = \delta\phi_2(x,y)$. These curves characterize a characteristic value of the mentioned discrepancies expressed in terms of the wave intensity and phase shift, which can be directly measured in experiments with laser shadowgraphy and interferometry. In addition, in Figs. 6*c* and 6*d* we plotted the errors $NRMSD[I_{1,2}; I_1]$ and $NRMSD\ [\delta\phi_{1,2}(x,y);\ \delta\phi_1(x,y)]$ on the basis of the computed expressions

$$NRMSD[I_{1,2}(x,y);I_1(x,y)]=\frac{\sqrt{\frac{1}{N_y}\sum_{k=0}^{N_y}[I_1(x_n,y_k)I_2(x_n,y_k)-I_1(x_n,y_k)]^2}}{\frac{1}{N_y}\sum_{k=0}^{N_y}I_1(x_n,y_k)}, \tag{22}$$

$$NRMSD[\delta\phi_{1,2}(x,y);\delta\phi_1(x,y)]=\frac{\sqrt{\frac{1}{N_y}\sum_{k=0}^{N_y}[\delta\phi_2(x_n,y_k)]^2}}{\max\{\delta\phi_1(x)\}-\min\{\delta\phi_1(x)\}}. \tag{23}$$

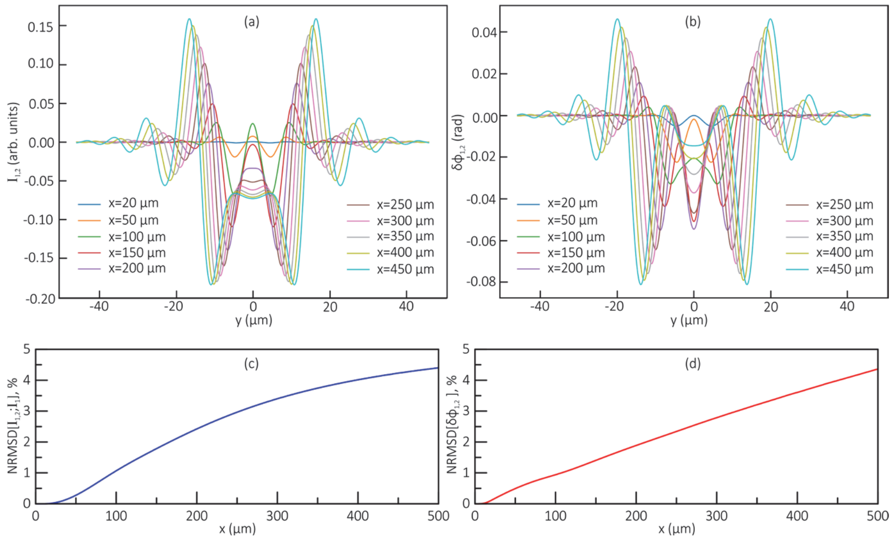

Fig. 6. The curves characterizing the discrepancy between the first and second terms of the complex phase series, which are expressed in terms of intensity $I_{1,2}(x,y)=I_1(x,y)\times I_2(x,y)-I_1(x,y)$ *(a) and phase shift* $\delta\phi_{1,2}(x,y)=\delta\phi_2(x,y)$

From the graphs in Figs. 6(*a*) and 6(*b*) it is evident that the functions $I_{1,2}$ and $\delta\phi_{1,2}$ are represented by a set of amplitude beats oscillating relative to the zero level. In the region of the object's output plane, the difference between the intensities $I_1\times I_2$ and I_1 is negligible together with the difference between the phase shifts $\delta\phi_1+\delta\phi_2$ and $\delta\phi_1$. This fact indicates a high accuracy of describing the wave passage through the object in the first Rytov approximation. As the diffracted wave propagates behind the object's output plane, the discrepancy between the indicated functions increases, but even on the scale of the computational region $\Delta X\times\Delta Y$, the corresponding discrepancies do not exceed 5 %, see Figs. 6*a* and 6*b*.

Thus, the direct problem of plane wave diffraction by an inhomogeneous plasma object is reliably described in terms of the first Rytov approximation. Together with the theory of solving the inverse problem, developed in [29], this allows one to precisely reconstruct spatial properties of the phase object under study and reveal its optical characteristics in detail.

4. Calculation of high order terms of the Rytov series

Further terms of the sum of an infinite series are found by substituting it into Eq. (5) and equating groups of terms of the same order of smallness to zero. The following system of equations is obtained

$$2ik\frac{\partial\Phi_2}{\partial x}+\Delta_\perp\Phi_2=-(\nabla_\perp\Phi_1)^2, \tag{24}$$

$$2ik\frac{\partial\Phi_3}{\partial x}+\Delta_\perp\Phi_3=-2\nabla_\perp\Phi_1\nabla_\perp\Phi_2, \tag{25}$$

$$2ik\frac{\partial\Phi_4}{\partial x}+\Delta_\perp\Phi_4=-((\nabla_\perp\Phi_2)^2+2\nabla_\perp\Phi_3\nabla_\perp\Phi_1), \tag{26}$$

$$2ik\frac{\partial\Phi_5}{\partial x}+\Delta_\perp\Phi_5=-(2\nabla_\perp\Phi_2\nabla_\perp\Phi_3+2\nabla_\perp\Phi_1\nabla_\perp\Phi_4). \tag{27}$$

From the right side of the equation, taken with a minus sign, the Fourier transform is taken as in Eq. (11). In a similar way to (12) , the Ψ_i, where $i=2,3,4,5..$ is obtained. The complex spatial phase for each of the subsequent terms of the Rytov approximation is found by taking the inverse Fourier transform, as in the case of the first term. When taking the real part from this phase, we get a level function for each of the terms, which we then recalculate into intensity. To account for the arbitrary Rytov approximation for intensity, it is necessary to multiply all its previous terms by each other and by this last term. The calculated wave phase in a certain approximation is obtained simply by adding of the imaginary parts of the spatial complex phases.

The left panel in the Fig. 7 shows the intensity differences between successive approximations (legend: blue – I_2-I_1, orange – I_3-I_2, green – I_4-I_3, red – I_5-I_4) along the horizontal coordinate x. The right panel in the Fig. 7 shows corresponding phase differences $\phi_2-\phi_1$, $\phi_3-\phi_2$, etc. The plots represent the residuals between adjacent terms of the expansion; therefore, their magnitude directly shows the contribution of each subsequent term to the final diffraction profile.

The figure shows that the most significant correction is given precisely by the second term of the expansion: the blue curve (the first correction to the intensity / phase difference between the first and second approximation) demonstrates the largest amplitude and localized perturbations in the region adjacent to the obstacle (including pronounced oscillations near the edges). The orange curve (the contribution of the third term relative to the second) is noticeable but is significantly smaller in amplitude than the blue one and mainly corrects finer features of the distribution. The green and red curves (contributions of the fourth and fifth terms) are almost invisible on the scale of the figure - they are negligible and only affect extremely minor, local details.

Thus, the rapid convergence of the expansion is visually confirmed: the second term provides a qualitatively significant improvement to the approximation, while all subsequent terms in the considered case of wavelength equals to 532 nm and normal incidence of a plane wave introduce only minor corrections. The practical conclusion is that for calculating diffraction on an object of this type, it is sufficient to account for the second term if higher accuracy is required; accounting for higher-order terms is advisable only when there is a need to describe extremely fine local fluctuations.

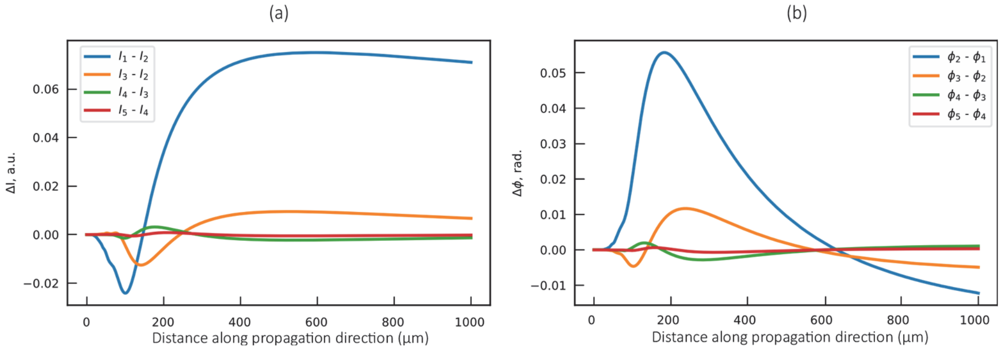

Fig. 7. Difference between brightness (a) and phase (b) of the wave diffracted by the plasma filament 20 μm in diameter at the center of the diffraction pattern ($y = 0$). The grid step is $\Delta = 0.75$ μm.The point $x = 0$ corresponds to the objects' input plane

Conclusion

In the study, we investigated in detail the features of the numerical calculation of diffraction equations obtained in the paradigm of the Rytov's approaches to solve the parabolic wave equation by using a complex phase function. The substantiated guides for determining the required spatial step of the computational grid are presented, and an empirical formula is obtained for setting the computational grid scale in the periphery for an optimal description of wave diffraction in the near-field region of the probed object. The convergence of the computed equations is investigated depending on various parameters of the numerical calculation. The two-dimensional brightness and phase patterns of the object are modeled using the first and second terms of the Rytov's series of a complex phase. Numerical results indicate a high accuracy of evaluating the diffraction patterns of plasma micron-sized objects in the field of coherent radiation in the framework of the first Rytov approximation. In turn, the findings can be of wide interest for the development of new precision methods of optical imaging rapidly evolving phase objects.

References

[1] Berwick B, Nugent KA, Williams GJ, et al. Keyhole coherent diffractive imaging. Nat Phys 2008; 4(5): 394-398. doi:10.1038/nphys896. [web:312]

[2] Popov NL, Artyukov IA, Vinogradov AV, Protopopov VV. Wave packet in the phase problem in optics and ptychography. Phys Usp 2020; 63(8): 766-774. doi:10.3367/UFNe.2020.05.038775. [web:316]

[3] Parkevich E, Khirianova A, Khirianov T, et al. Parameters of electric spark microchannels in the near-anode region of the discharge. Bull Lebedev Phys Inst 2023; 50(Suppl 11): S1283-S1286. doi:10.3103/S1068335623602029.

[4] Almazova K, Belonogov A, Borovkov V, et al. Investigation of the microchannel structure in the initial phase of the discharge in air at atmospheric pressure in the pin (anode)-plane gap. Phys Plasmas 2020; 27(11): 113502. doi:10.1063/5.0026192.

[5] Cui Y, Zhuang C, Zhou X, Zeng R. Dynamic expansion of leader discharge channels under positive voltage impulse with different rise times in long air gap: experimental observation and simulation results. J Appl Phys 2019; 125(11): 113303. doi:10.1063/1.5085852.

[6] Šimek M, Hoffer P, Tungli P, et al. Investigation of the initial phases of nanosecond discharges in liquid water. Plasma Sources Sci Technol 2020; 29(6): 064001. doi:10.1088/1361-6595/ab87b7.

[7] Ping Y, Geltner I, Morozov A, Suckewer S. Interferometric measurements of plasma density in microcapillaries and laser sparks. Phys Plasmas 2002; 9(11): 4756-4766. doi:10.1063/1.1510124.

[8] Wei W, Li X, Wu J, et al. Interferometric and schlieren characterization of the plasmas and shock wave dynamics during laser-triggered discharge in atmospheric air. Phys Plasmas 2014; 21(9): 093505. doi:10.1063/1.4893312.

[9] Yang Z, Wei W, Han J, et al. Experimental study of the behavior of two laser-produced plasmas in air. Phys Plasmas 2015; 22(8): 083505. doi:10.1063/1.4927587.

[10] Soto L, Pavez C, Castillo F, et al. Filamentary structures in dense plasma focus: current filaments or vortex filaments? Phys Plasmas 2014; 21(10): 103102. doi:10.1063/1.4886135.

[11] Polukhin S, Gurei A, Nikulin VY, et al. Studying how plasma jets are generated in a plasma focus. Plasma Phys Rep 2020; 46(2): 127-137. doi:10.1134/S1063780X20020087.

[12] Nicolai P, Stenz C, Kasperczuk A, et al. Studies of supersonic, radiative plasma jet interaction with gases at the Prague Asterix Laser System facility. Phys Plasmas 2008; 15(9): 093702. doi:10.1063/1.2963083.
[13] Harilal SS, Miloshevsky GV, Diwakar PK, et al. Experimental and computational study of complex shockwave dynamics in laser ablation plumes in argon atmosphere. Phys Plasmas 2012; 19(8): 083301. doi:10.1063/1.4745867.
[14] Pandey PK, Gupta SL, Thareja RK. Study of pulse width and magnetic field effect on laser ablated copper plasma in air. Phys Plasmas 2015; 22(8): 083301. doi:10.1063/1.4926528.
[15] Mao SS, Mao X, Greif R, Russo RE. Influence of preformed shock wave on the development of picosecond laser ablation plasma. J Appl Phys 2001; 89(7): 4096-4098. doi:10.1063/1.1351870.
[16] Gregorcic P, Mozina J. High-speed two-frame shadowgraphy for velocity measurements of laser-induced plasma and shock-wave evolution. Opt Lett 2011; 36(14): 2782-2784. doi:10.1364/OL.36.002782.
[17] Raclavský M, Rao KH, Chaulagain U, et al. High-sensitivity optical tomography of instabilities in supersonic gas flow. Opt Lett 2024; 49(8): 2253-2256. doi:10.1364/OL.510289.
[18] Khalid S, Kappus B, Weninger K, Putterman S. Opacity and transport measurements reveal that dilute plasma models of sonoluminescence are not valid. Phys Rev Lett 2012; 108(10): 104302. doi:10.1103/PhysRevLett.108.104302.
[19] de Bruyn JR, Bodenschatz E, Morris SW, et al. Apparatus for the study of Rayleigh–Bénard convection in gases under pressure. Rev Sci Instrum 1996; 67(6): 2043-2067. doi:10.1063/1.1147511.
[20] Gopal A, Minardi S, Tatarakis M. Quantitative two-dimensional shadowgraphic method for high-sensitivity density measurement of under-critical laser plasmas. Opt Lett 2007; 32(9): 1238-1240. doi:10.1364/OL.32.001238.
[21] Müller P. Optical diffraction tomography for single cells [PhD thesis]. Dresden: Technische Universität Dresden, Biotechnology Center; 2016.
[22] Chaumet PC, Sentenac A, Zhang T. Reflection and transmission by large inhomogeneous media: validity of Born, Rytov and beam propagation methods. J Quant Spectrosc Radiat Transf 2020; 243: 106816. doi:10.1016/j.jqsrt.2019.106816.
[23] Chen B, Stamnes JJ. Validity of diffraction tomography based on the first Born and the first Rytov approximations. Appl Opt 1998; 37(15): 2996-3006. doi:10.1364/AO.37.002996.
[24] Marks DL. Family of approximations spanning the Born and Rytov scattering series. Opt Express 2006; 14(19): 8837-8848. doi:10.1364/OE.14.008837.
[25] Sung Y, Barbastathis G. Rytov approximation for X-ray phase imaging. Opt Express 2013; 21(3): 2674-2682. doi:10.1364/OE.21.002674.
[26] Sung Y, Sheppard CJ, Barbastathis G, et al. Full-wave approach for X-ray phase imaging. Opt Express 2013; 21(15): 17547-17557. doi:10.1364/OE.21.017547.
[27] Parkevich E, Khirianova A, Khirianov T, et al. Strong diffraction effects accompany the transmission of a laser beam through inhomogeneous plasma microstructures. Phys Rev E 2024; 109(5): 055204. doi:10.1103/PhysRevE.109.055204.
[28] Parkevich EV, Khirianova AI, Khirianov TF, Gavrilov SY. Features of phase object visualization in the field of coherent laser radiation predicted in the first Rytov approximation. Computer Optics 2025; 49(4): 566-572. doi:10.18287/2412-6179-CO-1608.
[29] Parkevich EV, Khirianova AI, Khirianov TF. Solving of the inverse diffraction problem in the first Rytov approximation for retrieving the phase object dielectric permittivity. Computer Optics 2025; 49(5): 749-757. DOI: 10.18287/2412-6179-CO-1617.
[30] Tatarski VI. Wave propagation in a turbulent medium. Mineola, NY: Dover Publications; 2016.
[31] Rytov SM, Kravtsov YA, Tatarskii VI. Introduction to statistical radiophysics. Berlin: Springer; 1978.
[32] Parkevich EV, Medvedev MA, Ivanenkov GV, et al. Fast fine-scale spark filamentation and its effect on the spark resistance. Plasma Sources Sci Technol 2019; 28(9): 095003. doi:10.1088/1361-6595/ab3768. [web:315]

Author’s information

Sergei Yurievich Gavrilov (b. 2000), completed Bachelors’ (2022) degree in Physics from M.V. Lomonosov Moscow State University and Master’s (2024) degree in Applied Mathematics and Physics from Moscow Institute of Physics and Technology. Currently he works as a Junior Research Scientist at the P.N. Lebedev Physical Institute of the Russian Academy of Sciences (LPI RAS). E-mail: s.gavrilov@lebedev.ru

Aleksandra Igorevna Khirianova (b. 1990), completed Bachelors’ (2012) and Master’s (2014) degree in Applied Mathematics and Physics from Moscow Institute of Physics and Technology. Received his Ph.D. degree in Plasma Physics (2018). She works as a Research Scientist at the P.N. Lebedev Physical Institute of the Russian Academy of Sciences (LPI RAS). Her research interests include: laser plasma diagnostics, modeling of laser diffraction, and image processing. E-mail: hiryanovaai@lebedev.ru

Egor Vadimovich Parkevich (b. 1993), completed Bachelors’ (2015) and Master’s (2017) degree in Applied Mathematics and Physics from Moscow Institute of Physics and Technology (MIPT). Received his Ph.D. degree in Plasma Physics (2021). He works as a Senior Research Scientist at the P.N. Lebedev Physical Institute of the Russian Academy of Sciences (LPI RAS). His research interests include: laser plasma diagnostics, modeling of laser diffraction, and image processing. E-mail: parkevich@phystech.edu

Received on September 26, 2025. The final version – October 29, 2025.